



Effect of humidification on the performance of intermediate-temperature proton conducting ceramic fuel cells with ceramic composite cathodes

Ki-Chae Lee, Moon-Bong Choi, Dae-Kwang Lim, Bhupendra Singh, Sun-Ju Song*

Ionics Lab, School of Materials Science and Engineering, Chonnam National University, 300 Yongbong-dong, Buk-gu, Gwang-Ju 500-757, Republic of Korea

HIGHLIGHTS

- Effect of electrode humidity on fuel cell performance using composite cathode.
- Effect of composite cathode composition on fuel cell performance.
- Gives insight into water management in proton conducting ceramic fuel cells.

ARTICLE INFO

Article history:

Received 1 November 2012

Received in revised form

18 December 2012

Accepted 1 January 2013

Available online 18 January 2013

Keywords:

Intermediate temperature proton-conducting ceramic-electrolyte fuel cell

Yttrium-doped barium cerate

Tape casting

Ceramic composite cathode

ABSTRACT

The effect of variations in flow rate and the humidity content of the cathode and anode gases on the performance of $\text{BaCe}_{0.85}\text{Y}_{0.15}\text{O}_{3-\delta}$ electrolyte-based proton conducting ceramic fuel cell with ceramic composite cathodes are studied. Increased flow rate of gases has positive effect but the presence of humidity in the cathode/anode gases has negative effect on the performance. The effect of humidity is more pronounced when it is present in the cathode gas than when it is present in the anode gas. Also, the effect of humidity is dependent on the nature of the cathode material; in the case of $\text{La}_{0.8}\text{Sr}_{0.2}\text{MnO}_3\text{—Gd}_{0.1}\text{Ce}_{0.9}\text{O}_{1.95}$ cathode some of the reaction sites are occupied by H_2O vapor and which leads to increase in the charge transfer resistance. Replacing $\text{La}_{0.8}\text{Sr}_{0.2}\text{MnO}_3\text{—Gd}_{0.1}\text{Ce}_{0.9}\text{O}_{1.95}$ with $\text{La}_{0.8}\text{Sr}_{0.2}\text{MnO}_3\text{—BaCe}_{0.85}\text{Y}_{0.15}\text{O}_{3-\delta}$ cathode leads to an increase in the effective area of three phase boundary, which mitigates the adverse effects of humidity to a certain extent.

© 2013 Elsevier B.V. All rights reserved.

1. Introduction

Solid oxide fuel cells are capable of operating on conventional fuels as well as on hydrogen and have suitable perspectives to replace their classical counterparts for the distributed generation of electrical energy with small and medium power sources with the advantage of high conversion efficiency and low environmental impact. The main issue for the widespread application of solid oxide fuel cells, however, is high operating temperature ($>800^\circ\text{C}$) and the resulting materials and cost limitations and operating complexities [1,2]. Therefore, the lowering of operating temperature of solid oxide fuel cells (SOFCs) to the intermediate range

($500\text{--}800^\circ\text{C}$) has become one of the main goals in SOFC research [3–5].

In the recent years, proton conducting ceramic oxide electrolytes has attracted the attention of SOFC research because of their appreciably high proton conductivity in the intermediate temperature range [5–12]. In dependence of their lower activation energy for the proton conduction [13,14], these proton conducting ceramic oxide fuel cells (PCFCs) can operate in the temperature range of $400\text{--}750^\circ\text{C}$. While operating on hydrogen fuel, the PCFCs offer added advantage over oxide ion conducting electrolyte based SOFCs by generating water at the cathode, and, thus overcoming the problem of fuel dilution [15]. Barium cerate (BaCeO_3) based materials have been considered as good electrolytes because of their high proton conductivity in the intermediate temperature range [16–20] and many perovskite-type mixed ionic and electronic conductors, such as $\text{La}_x\text{Sr}_{1-x}\text{Co}_y\text{Fe}_{1-y}\text{O}_{3-\delta}$ [21,22], $\text{Ba}_{0.5}\text{Sr}_{0.5}\text{Co}_{0.8}\text{Fe}_{0.2}\text{O}_{3-\delta}$ [23], $\text{Sm}_{0.5}\text{Sr}_{0.5}\text{CoO}_{3-\delta}$ [24], and Pr-doped BaCo_2O_5 ($\text{PrBaCo}_2\text{O}_{5+\delta}$) [25] and Gd-doped BaCo_2O_5 ($\text{GdBaCo}_2\text{O}_{5+\delta}$) [26] as

* Corresponding author. School of Materials Science and Engineering, Chonnam National University, 300 Yongbong-dong, Buk-gu, Gwang-Ju 500-757, Republic of Korea. Tel.: +82 62 530 1706; fax: +82 62 530 1699.

E-mail address: song@chonnam.ac.kr (S.-J. Song).

potential cathode materials and Ni-cermet [27,28] as potential anode materials in the intermediate temperature operations of PCFCs. In general, however, no matter which material is used as electrode, high polarization resistance has been major concern for the operation at the intermediate temperatures. The polarization resistance may include the contributions from – (1) low diffusivity of hydrogen at anode substrate (AS)/anode functional layer (AFL) interlayer, (2) hydrogen dissociation reaction at anode, (3) proton transport through solid–solid hetero junction of electrolyte/electrode interface and (4) reaction of $2\text{H}^+ + 1/2\text{O}_2 \rightarrow \text{H}_2\text{O}$ at the three phase boundary (TPB) of electrolyte–cathode–gas [29]. Clearly, the polarization resistance of the cell is dependent on the gas conditions at cathode and anode and in many cases the cathodic polarization is the dominant factor in total polarization resistance [29,30].

Unlike the oxide ion conductors, where ionic conductivity comes from the oxide ions intrinsic to the material, the proton conducting solid electrolytes themselves do not have structural protons and their proton conductivity arise from the incorporation of protons from the external means such as from H_2 or moisture. Therefore, any variation in the conditions which affect the incorporation of protons into the PCFC electrolytes would lead to the variations in the performance of PCFCs. Also, during the operation of PCFCs water is formed at cathode and therefore, the management of water and humidity conditions of the various gases supplied at the electrodes could affect the electrode polarization and this, in turn, could be an important factor in deciding the overall performance of the intermediate temperature-PCFCs (IT-PCFCs) in humid atmosphere. Therefore, in the present study we have intended to analyze the effect of variation of gas flow rate and humidity conditions on the electrodes on the overall performance of the IT-PCFCs. We fabricated a Y-doped barium cerate $\text{BaCe}_{0.85}\text{Y}_{0.15}\text{O}_{3-\delta}$ (BCY15) electrolyte-based fuel cell and measured its performance in different gas flow rate with vapor pressure conditions ($P_{\text{H}_2\text{O}}$) at cathode and anode, while using hydrogen as a fuel. A single-cell was fabricated by using NiO–BCY15 as anode, BCY15 as electrolyte and $\text{La}_{0.8}\text{Sr}_{0.2}\text{MnO}_3\text{--Gd}_{0.1}\text{Ce}_{0.9}\text{O}_{1.95}$ (LSM–GDC) cathode. The purpose of choosing BCY15 as electrolyte, instead of $\text{BaCe}_{0.80}\text{Y}_{0.20}\text{O}_{3-\delta}$ (BCY20) or other $\text{BaCe}_{1-x}\text{Y}_x\text{O}_{3-\delta}$ with higher Y content, was to ensure high proton conductivity and, at the same time, to avoid the solubility limit of yttrium in BaCeO_3 (viz. 20% in $\text{BaCe}_{1-x}\text{Y}_x\text{O}_{3-\delta}$) [31] and to minimize the partial conversion of rhombohedral structure to a monoclinic structure, for the composition range of $0.15 \leq x \leq 0.25$ where maximum total conductivity is observed, upon exposure to H_2O - or H_2 -containing atmospheres [32], while analyzing the effect of the variations in the parameters under study. NiO–BCY15 was used as anode. The use of composite cathodes in SOFCs has led to the lowering of electrode overpotential by allowing the extension of TBP from electrolyte/cathode interface to the whole cathode bulk [33–35]. There are many reports of the use of LSM–GDC composite cathodes in oxide ion conducting electrolyte based SOFCs [33,34], in the present study we utilized LSM–BCY15 as well as LSM–GDC composite as cathode in IT-PCFC. There are a few reports about the effect of humidity at the electrodes on the performance of PCFC using metallic electrodes [36], in the present work we used ceramic composite (LSM–GDC and LSM–BCY15) as cathodes and NiO–BCY15 cermet as anode for the study, as they present advantage of better compatibility with ceramic electrolyte and lower material-cost. Also, by taking two different composite cathodes–LSM–GDC, which has oxide ion conductor component GDC, and LSM–BCY15, which has predominantly proton conductor component BCY15, at the temperature under study, we have tried to compare their performances in IT-PCFC. The single cell performance was measured using hydrogen as fuel with different cathodes and different water

vapor condition of the cathode and anode gases at 750 °C. The power density and voltage was measured by varying the humidity condition of the various gases supplied at the electrodes.

2. Experimental

2.1. Fabrication of single button cell

The flow chart of the different steps involved in the fabrication of a single button cell is shown in Fig. 1(A). In order to get porous anode support, polycrystalline BCY15 powders with small BET surface area were prepared by the conventional solid state reaction method. The high purity oxide powders of BaCO_3 (99.8%, Alfa Aesar), CeO_2 (99.9%, Alfa Aesar) and Y_2O_3 (Sigma Aldrich, 99.99%) were mixed in weighted stoichiometric amounts of components and the mixture was planetary ball-milled for 3 h with ethanol solvent in a Teflon jar at 200 rpm. The ball-milled mixture was calcined at 1400 °C for 10 h in air to get BCY15. The calcined powder was again grinded with mortar and pestle to get as-prepared BCY15 powder for the further use in the fabrication of AS.

The porous NiO–BCY15 AS was prepared by tape-casting method [37,38]. A slurry of NiO (Kceracell; $\text{BET} = 4\text{--}6 \text{ m}^2 \text{ g}^{-1}$, $d_{50} = 0.3\text{--}0.6 \mu\text{m}$; where BET and d_{50} represent Brunauer–Emmett–Teller surface area and mean particle size, respectively) and as-prepared BCY15 ($\text{BET} = 0.94 \text{ m}^2 \text{ g}^{-1}$, $d_{50} = 0.58 \mu\text{m}$) mixture, in 1:1 vol. ratio, was prepared in two steps. Firstly, NiO and as-prepared BCY15 powders were dispersed in a binary solvent system (toluene:ethyl alcohol = 1:1 wt. ratio) with fish oil (Aldrich) as a dispersant by ball-milling for 24 h. Butyl benzyl phthalate (Ferro) and polyethylene glycol (PEG 8000, Acros) were added as plasticizers and polyvinyl butyral (Butvar) was added as a binder, and the whole mixture was again ball-milled for 24 h. The de-airing process was conducted to avoid the defects caused by the air bubbles in the slurry. Then the NiO–BCY15 AS tapes were fabricated by tape-casting process and the obtained green sheet (thickness; about 350 μm) was cut in the form of 25 mm diameter circles by punching and, finally, the cut circular anode tapes were sintered stepwise-at (i) 200 °C for 2 h, (ii) 400 °C for 2 h and (iii) 1000 °C for 2 h.

For the fabrication of the AFL, a coating slurry of NiO (Kceracell; $\text{BET} = 8\text{--}12 \text{ m}^2 \text{ g}^{-1}$, $d_{50} = 0.2\text{--}0.5 \mu\text{m}$) and commercially available BCY15 (Kceracell; $\text{BET} = 8.5 \text{ m}^2 \text{ g}^{-1}$, $d_{50} = 0.14 \mu\text{m}$) mixture was prepared in ethanol based solvent following the procedure already reported elsewhere [39] and was coated onto the as-sintered AS by dip-coating method to form AFL on AS (AS/AFL). The AS/AFL samples were heat-treated at 400 °C for 2 h to burn out the organic materials present in the coating slurry. The electrolyte coating slurry was also prepared in an ethanol based solvent and commercially available BCY15 (Kceracell; $\text{BET} = 8.5 \text{ m}^2 \text{ g}^{-1}$, $d_{50} = 0.14 \mu\text{m}$) and the BCY15 electrolyte layer was coated onto the as-prepared AS/AFL sample by dip-coating method following the procedure already reported elsewhere [39]. Finally, the whole set-up of AS/AFL/electrolyte was sintered at 1400 °C for 5 h in air atmosphere. The linear shrinkage rate along the diameter of sintered sample was ~20%.

A mixture of $\text{La}_{0.8}\text{Sr}_{0.2}\text{MnO}_3$ (LSM, Kceracell, $\text{BET} = 5\text{--}10 \text{ m}^2 \text{ g}^{-1}$, $d_{50} = 0.3\text{--}0.6 \mu\text{m}$) and $\text{Gd}_{0.1}\text{Ce}_{0.9}\text{O}_{1.95}$ (GDC, Kceracell, $\text{BET} = 5\text{--}8 \text{ m}^2 \text{ g}^{-1}$, $d_{50} = 0.3\text{--}0.5 \mu\text{m}$) in 1:1 wt. ratio was used as the cathode material. The LSM–GDC paste was prepared using planetary centrifugal mixer (Thinky Mixer AR-100) with a texanol-based vehicle (type-441, ESL). The LSM–GDC mixture was coated on the as-sintered set-up of AS/AFL/electrolyte by screen printing method to complete the button cell and, finally, the button cell assembly was fired at 1150 °C for 2 h. The button cell assembly with LSM–BCY15 cathode was fabricated in the similar manner using LSM and commercially available BCY15 in 1:1 wt. ratio.

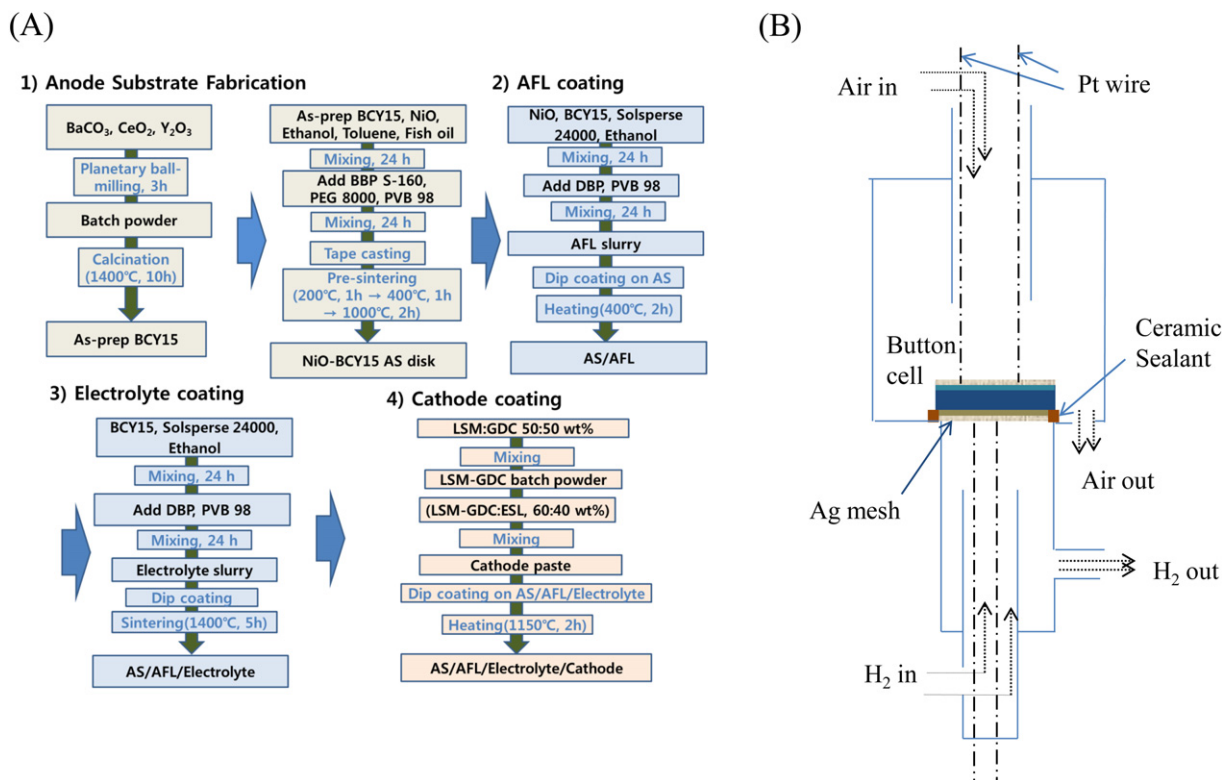


Fig. 1. (A) The flow chart of the different steps involved in the fabrication of a single button cell, (B) The schematic diagram of IT-PCFC testing assembly for *dc* conductivity measurement at 750°C . Various abbreviations used in Fig. 1(A) are: BCY15 → $\text{BaCe}_{0.85}\text{Y}_{0.15}\text{O}_{3-\delta}$; BBP S-160 → butyl benzyl phthalate; PEG 8000 → polyethylene glycol; PVB 98 → polyvinyl butyral; AS → anode support; AFL → anode functional layer; DBP → dibutyl phthalate; ESL → texanol-based vehicle (type-441); LSM → $\text{La}_{0.8}\text{Sr}_{0.2}\text{MnO}_3$; and GDC → $\text{Gd}_{0.1}\text{Ce}_{0.9}\text{O}_{1.95}$.

2.2. Physical characterization

The crystalline phases of the calcined powder and the crushed sintered disks were examined using an X-ray diffractometer (XRD-7000, Shimadzu), which was equipped with a CuK_α radiation source (1.5406 \AA) and operated at 40 kV and 30 mA at a scan rate of 1°min^{-1} between scanning angles (2θ) of 10 and 90° . The pseudo-Voigt function was adopted as the profile function in Rietveld refinement computation. The microstructure of powder and sintered pellet was analyzed using a field-emission scanning electron microscope (FE-SEM, S-4700, Hitachi). The surface area of the as-prepared BCY15 was determined by surface area analyzer (ASAP 2020, Micrometrics Ins.) and d50 of the as-prepared BCY15 was measured by dynamic light scattering spectrophotometer (DLS-7000 AL, Otsuka Electronics).

2.3. Fuel cell tests

The button cell performance was evaluated at 750°C with different cathodes in different $P_{\text{H}_2\text{O}}$ and gas flow rate conditions, while using H_2 as fuel and air as oxygen source. The fuel side was sealed with a high temperature ceramic adhesive (Aremco Ceramabond™ 571). Silver mesh connected with Pt wires was used as voltage and current probes during *I*–*V* measurements and as current collectors during the electrochemical impedance spectroscopy (EIS) measurements. *I*–*V* measurements and the EIS were carried out using a potentiostat (Reference 3000, Gamry Instruments). The $P_{\text{H}_2\text{O}}$ was controlled by passing the gases through water kept at the different temperatures in a water bath. The experimental set-up for the fuel cell testing is schematically shown in Fig. 1(B).

3. Results and discussion

3.1. Phase and microstructure studies

The X-ray diffraction (XRD) pattern of as-prepared BCY15 powder calcined in air at 1400°C for 10 h is shown in Fig. 2. The

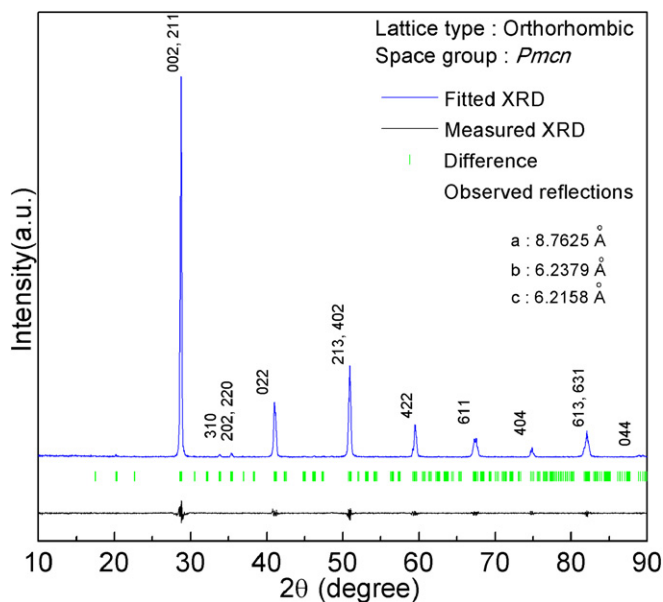


Fig. 2. Rietveld fit to the XRD spectra of as-prepared BCY15 sample using orthorhombic perovskite structure.

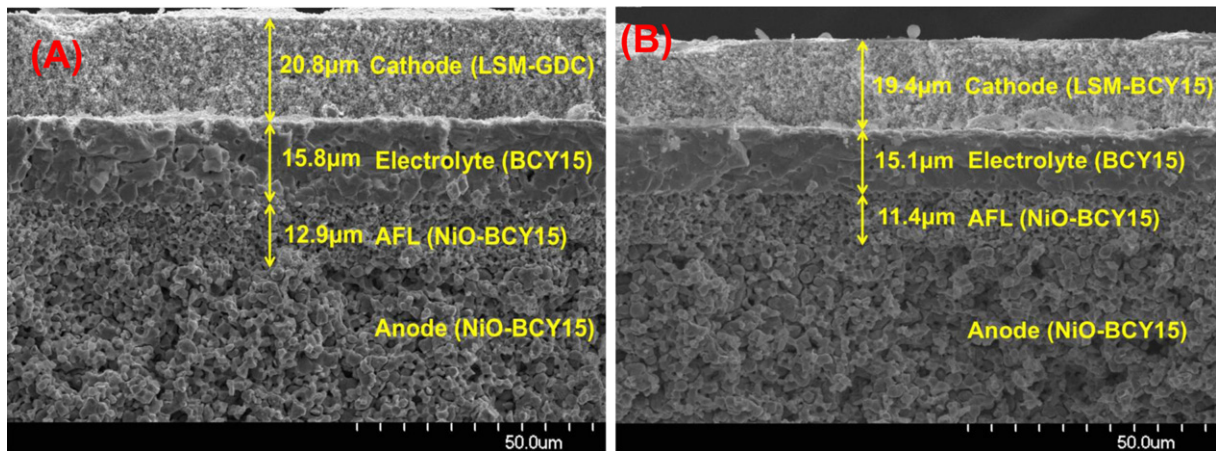


Fig. 3. SEM micrographs of cross-section of button cell with (A) LSM–GDC cathode and (B) LSM–BCY15 cathode.

XRD peaks confirm that the as-prepared BCY15 sample exhibits a single phase with the orthorhombic perovskite structure. The Rietveld refinement result obtained using orthorhombic lattice with $Pm\bar{c}n$ space group gives lattice parameters of $a = 8.7625 \text{ \AA}$, $b = 6.2379 \text{ \AA}$ and $c = 6.2158 \text{ \AA}$. For the as-prepared BCY15, the BET surface area was $0.94 \text{ m}^2 \text{ g}^{-1}$ and d_{50} was 0.58 μm .

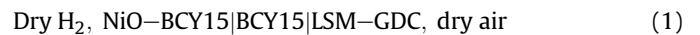
The scanning electron micrograph (SEM) of the cross-section of the button cell-assembly with (A) LSM–GDC cathode and (B) LSM–BCY15 cathode is shown in Fig. 3. In the button cell-assembly with LSM–GDC cathode, the thicknesses of AFL, electrolyte and cathode are 12.9 μm , 15.8 μm and 20.8 μm , respectively. On the other hand, in the button cell-assembly with LSM–BCY15 cathode, the thicknesses of AFL, electrolyte and cathode is 11.4 μm , 15.1 μm and 19.4 μm , respectively. The SEM micrograph indicates that the NiO–BCY15 anode substrate and functional layer, as well as LSM–GDC and LSM–BCY15 cathodes, has enough porosity for gas diffusion and the BCY15 electrolyte layer is highly dense and lacks the presence of the open pores, and, also, there is a good state of adhesion between cathode and the electrolyte layer.

3.2. Electrochemical studies

3.2.1. Effect of varying the gas flow rate at the electrodes

The effect of gas flow rate on the performance of the IT-PCFC is studied using two different cathodes: LSM–GDC and LSM–BCY15.

Firstly, the fuel cell test is performed with LSM–GDC cathode using a cell assembly (1) given below,



The effect of variations in gas flow rate on the voltage and the power density of the IT-PCFC, while supplying hydrogen at the anode and dry air at the cathode, are shown in Fig. 4(A). The value of theoretical OCV for the above cell is 1.358 V , however, the values of measured OCVs are $<0.95 \text{ V}$. The reason for the lower value of measured OCV could be cell cross-over, slow electrode kinetics and internal shorting in the fuel cell. There is an increase in the measured value of OCV and the maximum power density with increasing gas flow rate from 50 standard cubic centimeters (sccm) to 200 sccm. The maximum power density is $0.279, 0.316, 0.336$ and 0.394 W cm^{-2} , and measured OCV is $0.926, 0.933, 0.935$ and 0.941 V with the gas flow rate of 50, 100, 150 and 200 sccm respectively. The increase in gas flow rate can induce faster diffusion of the gases into the electrodes and which may leads to better utilization of fuel and subsequent increase in the maximum power density. Similarly, the increased diffusion of gases with the increasing flow rate leads to the better availability of gases at the TPB and slightly increases the vapor pressure of these gases at the TPB and which leads to an increase in voltage, as according to the Nernst equation [40]

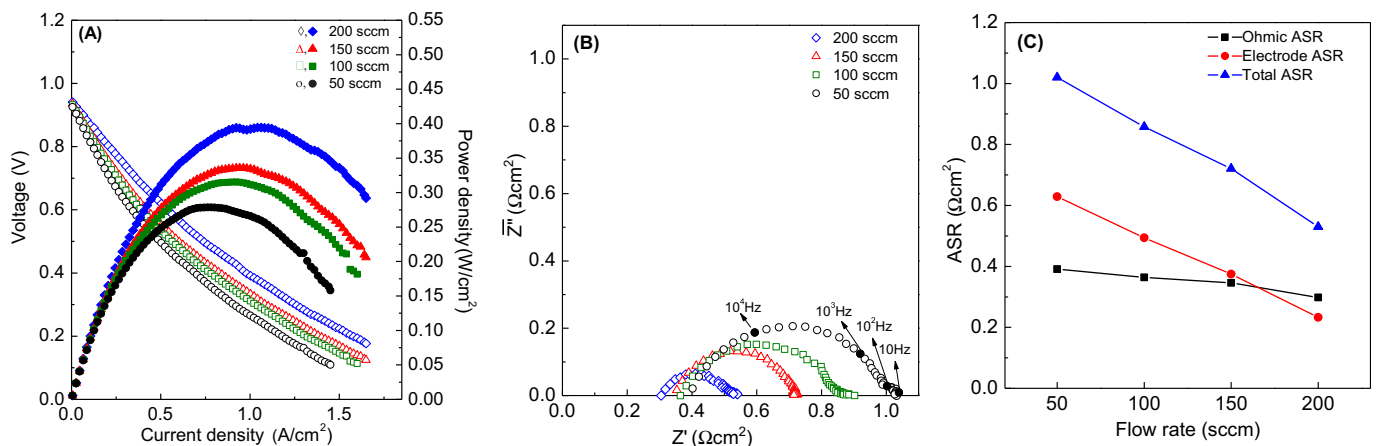


Fig. 4. Variation of (A) power density and OCV, (B) impedance response and (C) ASR with gas flow rates at the electrodes while using LSM–GDC cathode. The closed symbols in (A) represent data of power densities and the open symbols represent data of the voltage. Measurements were performed at 750 °C and, dry air and dry hydrogen were supplied at the cathode and anode respectively.

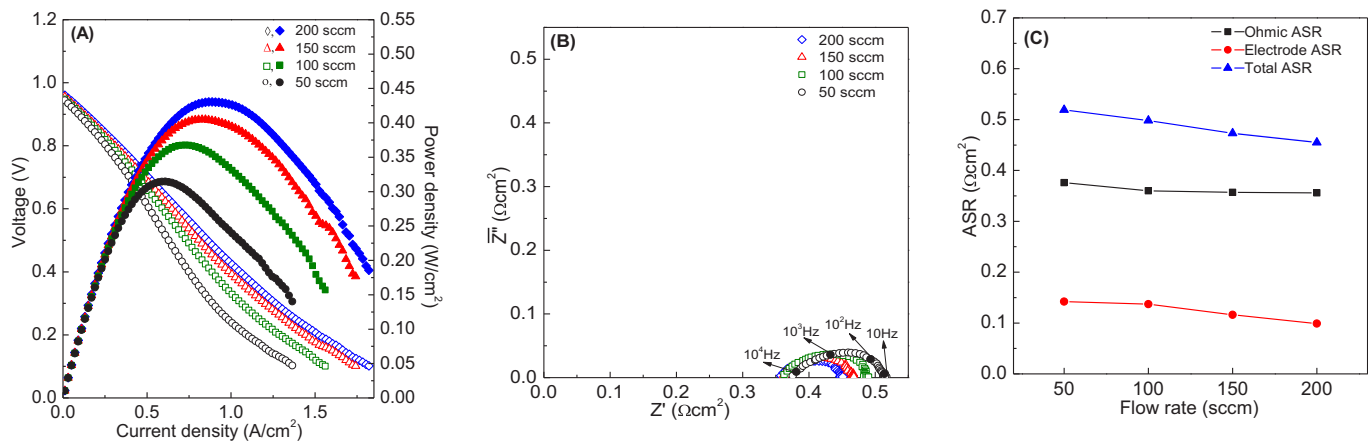


Fig. 5. Variation of (A) power density and OCV, (B) impedance response and (C) ASR with gas flow rates at the electrodes while using LSM–BCY15 cathode. The closed symbols in (A) represent data of power densities and the open symbols represent data of the voltage. Measurements were performed at 750 °C and, dry air and dry hydrogen were supplied at the cathode and anode respectively.

(Eq. (2)) given below, where E , E^0 , R , F , P_{H_2O} , P_{H_2} and P_{O_2} represent cell voltage, standard cell potential, the universal gas constant, the Faraday constant, water partial pressure, hydrogen partial pressure and oxygen partial pressure, respectively,

$$E = E^0 - \frac{RT}{2F} \ln \left(\frac{P_{H_2O}}{P_{H_2} P_{O_2}^{1/2}} \right) \quad (2)$$

The impedance response of the IT-PCFC at OCV, as shown in Fig. 4(B), reveals a low frequency semicircle and a high frequency intercept on the real axis corresponding to the polarization resistance (R_p) and the ohmic resistance (R_o) respectively. Fig. 4(C) shows the variation of area specific resistance (ASR) with the flow rate. As it is evident from Fig. 4(B) and (C), although there is small decrease in the value of R_o with the increasing the gas flow rate, the value of R_p decreases considerably with the increasing the gas flow rate. This decrease in polarization resistance can be attributed to the increase in availability of H_2 and O_2 at their respective TPB, because of increased convective mass-transfer through the flow channels inside the porous electrodes with the increasing gas flow rate. Although the values of P_{H_2} and P_{O_2} with different flow rate can be

considered as constant throughout the supply channels, the values of these parameters are non-uniform and vary throughout along the flow passages through the porous electrodes. Generally, these values are less in magnitude inside the porous electrodes than those along the supply channels due to the greater gas-phase mass-transfer resistance inside the narrow flow passages in the porous electrodes. On increasing the gas flow rate, convective mass-transfer through the flow channels inside the porous electrodes is increased and leads to concentration changes at TPB and, also, the rate at which the reactants are used and the product is removed. Therefore, increase in flow rate not only helps in increasing OCV but also it will be helpful in increasing power density, especially at high current densities. Also, during the operation of PCFC at 750 °C, water formed at cathode will be in the form of vapors, and its rapid removal from cathode would be crucial factor in deciding fuel cell performance. The increase in gas flow rate at cathode may help in rapid removal of water vapors from cathode and, thereby, ensuring lower cathode polarization resistance. The decrease in the ASR also leads to an increase in the maximum current density from 1.44 A cm^{-2} to 1.69 A cm^{-2} with the increasing gas flow rate from 50 sccm to 200 sccm.

The effect of flow rate on the performance of the IT-PCFC is also studied by changing the composition of cathode and fuel cell tests

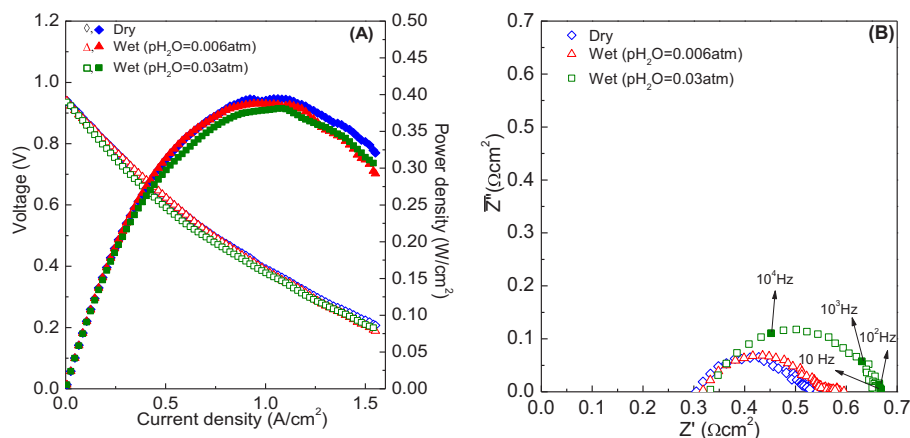


Fig. 6. Effect of variation of humidity in cathode gas (air) while using LSM–GDC cathode. (A) Variation of voltage and power density vs. current density, (B) variation of EIS response. The closed symbols in (A) represent data of power densities and the open symbols represent data of the voltage. Measurements were performed at 750 °C and dry H_2 was used as fuel on the anode side.

Table 1

Variation of OCV and ASR with the variation of humidity in cathode gas at 750 °C.

Type of cathode	Cathode gas condition	Theoretical OCV (V)	Measured OCV (V)	Ohmic ASR ($\Omega \text{ cm}^2$)	Electrode ASR ($\Omega \text{ cm}^2$)	Total ASR ($\Omega \text{ cm}^2$)
LSM–GDC	Dry	1.358	0.941	0.298	0.233	0.530
	Wet ($p_{\text{H}_2\text{O}} = 0.006 \text{ atm}$)	1.358	0.940	0.311	0.247	0.558
	Wet ($p_{\text{H}_2\text{O}} = 0.03 \text{ atm}$)	1.357	0.936	0.331	0.333	0.664
LSM–BCY15	Dry/Dry	1.358	0.961	0.356	0.099	0.455
	Wet ($p_{\text{H}_2\text{O}} = 0.03 \text{ atm}$)	1.357	0.955	0.360	0.111	0.471

are performed with LSM–BCY15 cathode using a cell assembly (3) given below,

Dry H_2 , NiO–BCY15|BCY15|LSM–BCY15, dry air (3)

The effect of variation in gas flow rate on the performance of the IT-PCFC, while using LSM–BCY15 as cathode, is shown in Fig. 5(A). The maximum power density is 0.315, 0.368, 0.405 and 0.43 W cm^{-2} , and the OCV is 0.945, 0.948, 0.955 and 0.961 V with the gas flow rate of 50, 100, 150 and 200 sccm respectively. The response of varying the gas flow rate at the electrodes while using LSM–BCY15 cathode is similar to that obtained while using LSM–GDC cathode, however, the values of maximum power density and OCV using LSM–BCY15 cathode are higher than those obtained using LSM–GDC cathode. Fig. 5(B) shows impedance response of the IT-PCFC at OCV and Fig. 5(C) shows variation of ASR with the variation in flow rate. When compared with the results obtained using LSM–GDC cathode, the values of electrode ASR using LSM–BCY15 cathode are significantly lower than the values obtained while using LSM–GDC cathode. Because of the presence of a common component (viz. BCY15), the LSM–BCY15 cathode and BCY15 electrolyte layers have better compatibility with each other during sintering, which may help imparting some homogeneity to the electrolyte/cathode interface and decreases interfacial resistance. Also, use of LSM–BCY15 cathode increases the effective area of TPB and reduces polarization resistance. As it is already mentioned that in many cases the cathodic polarization is the dominant factor in total polarization resistance [29,30], better compatibility of LSM–BCY15 cathode with BCY15 electrolyte could help reducing the cathodic polarization resistance and, thereby, improving the fuel cell performance. The decrease in polarization resistance leads to an increase in the maximum current density from 1.36 A cm^{-2} to

1.82 A cm^{-2} while increasing gas flow rate from 50 sccm to 200 sccm, as shown in Fig. 5(A).

3.2.2. Effect of the presence of humidity in the cathode gas

During the operation of IT-PCFCs, water is formed at the cathode and the management of this water has been important factor in deciding the overall performance of the fuel cell. Therefore, the selection of cathode which could effectively manage water vapor can be an important factor in better performance of IT-PCFCs. In the present study, we select two different cathodes having different components and species involved in ionic conduction; oxide ion conducting GDC in LSM–GDC and proton conducting BCY15 in LSM–BCY15, and by supplying the humid air at the cathode, we assess the performance of the PCFC. Firstly, the fuel cell tests are performed with LSM–GDC cathode using a cell assembly (4) given below,

Dry H_2 , NiO–BCY15|BCY15|LSM–GDC, wet air (4)

The effect of the presence of water vapor in the cathode gas on the performance of the IT-PCFC, while supplying dry hydrogen at the anode, is shown in Fig. 6(A). The values of maximum power density and OCV decrease with the increasing $p_{\text{H}_2\text{O}}$ in the cathode gas. This clearly shows that the presence of water vapor in the cathode gas has a negative effect on the performance of the IT-PCFC. Fig. 6(B) shows the impedance response of the IT-PCFC at OCV and the corresponding variations of area specific resistance (ASR) with the variation in $p_{\text{H}_2\text{O}}$ in cathode gas are given in Table 1. There is an increase in the electrode ASR with the increasing $p_{\text{H}_2\text{O}}$, which can be explained on the basis of hindrance created by the water molecules. In the presence of humidity, water molecules will occupy some of the reaction sites at the TPB and, therefore, leads to

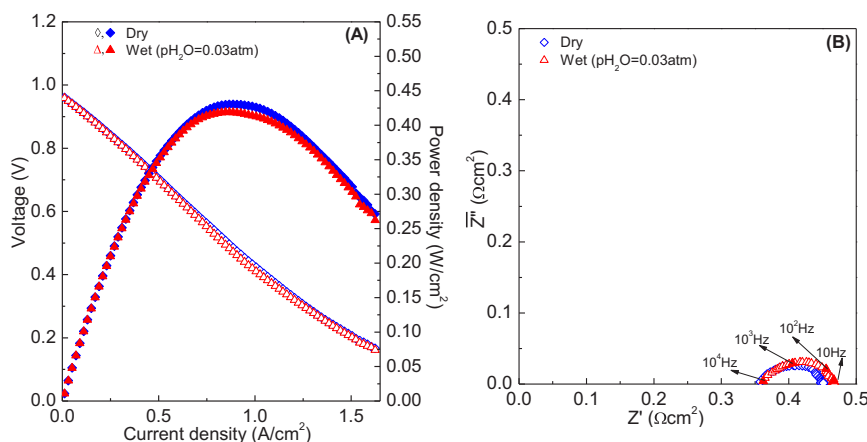


Fig. 7. Effect of variation of humidity in cathode gas (air) while using LSM–BCY15 cathode. (A) Variation of voltage and power density vs. current density, (B) variation of EIS response. The closed symbols in (A) represent data of power densities and the open symbols represent data of the voltage. Measurements were performed at 750 °C and dry H_2 was used as fuel on the anode side.

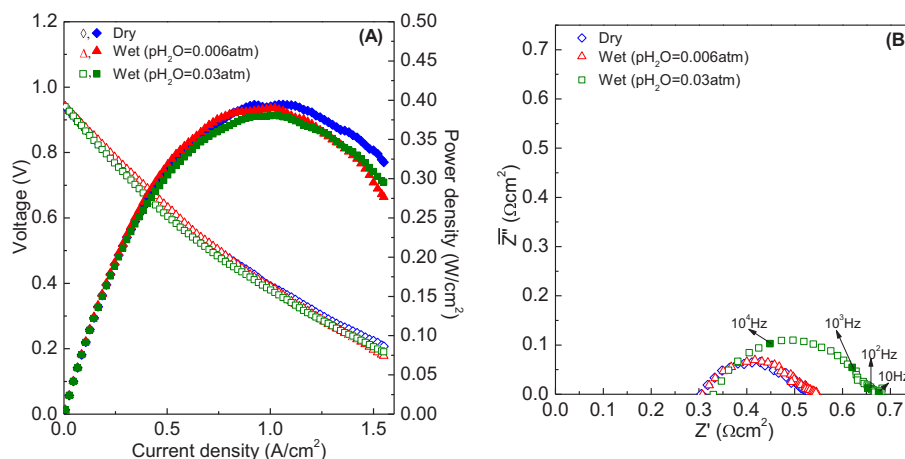


Fig. 8. Effect of variation of humidity in the anode gas (H_2 fuel) while using LSM–GDC cathode. (A) Variation of voltage and power density vs. current density and (B) variation of EIS response. The closed symbols in (A) represent data of power densities and the open symbols represent data of the voltage. Measurements were performed at 750°C and dry air was used on the cathode side.

increase in the polarization resistance. There is a strong possibility that in the presence of humidity some of water molecules will diffuse through the electrode pores and reach the TPB, therefore, leaving lesser space for O_2 molecules to avail reaction sites at the TPB. Also, there is an increase in the ohmic ASR in the presence of humidity (Table 1). Although BCY15 is a predominantly proton conductor at the higher temperatures, but in the intermediate temperature range $<800^\circ\text{C}$, it shows mixed oxide-ion and proton conductivity. Therefore, in the present measurement conditions ($T = 750^\circ\text{C}$) the contribution of oxide ion conduction in the total conductivity of the BCY15 electrolyte cannot be ignored and, in the presence of water vapor, it is possible that some water molecules may also diffuse into the BCY15 electrolyte and consume some oxygen vacancies ($V_o^{\bullet\bullet}$), as shown in Eq. (5) where different symbols have standard Kröger–Vink notation meaning, which results in an increase the ohmic ASR.



The fuel cell tests are also performed with LSM–BCY15 cathode using a cell assembly (6) given below,



The effect of the presence of water vapor in the cathode gas on the performance of the IT-PCFC, while supplying dry hydrogen at the anode, is shown in Fig. 7(A). There is a decrease in the maximum power density and OCV in the presence of H_2O vapor in the cathode gas, although the effect is less pronounced than that in the case of LSM–GDC. The impedance response of the IT-PCFC at OCV in Fig. 7(B) and the corresponding variations of ASR with the variation of P_{H_2O} in cathode gas are given in Table 1. Even with the LSM–BCY15

cathode, there is an increase in the electrode ASR in the presence of water vapor in the cathode gas. However, the comparison of the results in Figs. 5 and 6 shows that effect of humidity is less severe in the case of LSM–BCY15 cathode, because the use of BCY15 in the composite cathode extends the TPB toward the cathode bulk and helps minimizing the increase in polarization resistance due to the occupying of some of the reaction sites by water molecules.

3.2.3. Effect of the presence of humidity in the anode gas

While studying the effect of the presence of water vapor in the anode gas, we select two different cathodes: (1) LSM–GDC and (2) LSM–BCY15, and by supplying wet H_2 at the anode and dry air at the cathode, we assess the performance of the PCFC. Firstly, the fuel cell tests are performed with LSM–GDC cathode using a cell assembly (7) given below,



The effect of the presence of water vapor in the anode gas on the performance of the IT-PCFC with LSM–GDC cathode, while supplying dry air at the cathode, is shown in Fig. 8(A). The presence of water vapor in the anode gas has insignificant effect on the values of OCV and maximum power density. Fig. 8(B) shows the impedance response of the IT-PCFC at OCV and the corresponding variations of ASR with the variation of P_{H_2O} in anode gas are given in Table 2. There is an increase in the electrode ASR with the increasing pH_2O , which can be due to the interference by H_2O molecules in the diffusion of fuel gas at the TPB, as already mentioned in the case of humidification of cathode gas in the Section 3.2.2.

The fuel cell tests are also performed with LSM–BCY15 cathode using a cell assembly (8) given below,

Table 2
Variation of OCV and ASR with the variation of humidity in the anode gas at 750°C .

Type of cathode	Anode gas condition	Theoretical OCV (V)	Measured OCV (V)	Ohmic ASR ($\Omega \text{ cm}^2$)	Electrode ASR ($\Omega \text{ cm}^2$)	Total ASR ($\Omega \text{ cm}^2$)
LSM–GDC	Dry	1.358	0.941	0.298	0.233	0.530
	Wet ($pH_2O = 0.006 \text{ atm}$)	1.178	0.941	0.308	0.239	0.547
	Wet ($pH_2O = 0.03 \text{ atm}$)	1.107	0.940	0.332	0.323	0.654
LSM–BCY15	Dry	1.358	0.961	0.356	0.099	0.455
	Wet ($pH_2O = 0.03 \text{ atm}$)	1.107	0.959	0.359	0.109	0.468

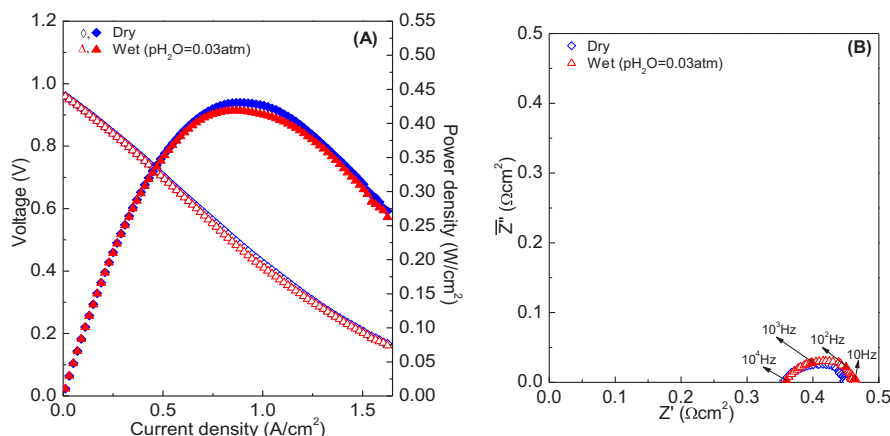


Fig. 9. Effect of variation of humidity in anode gas (H_2 fuel) while using LSM–BCY15 cathode. (A) Variation of voltage and power density vs. current density and (B) variation of EIS response. The closed symbols in (A) represent data of power densities and the open symbols represent data of the voltage. Measurements were performed at 750°C and dry air was used on the cathode side.

Wet H_2 , NiO–BCY15|BCY15|LSM–BCY15, dry air (8)

The effect of the presence of water vapor in the anode gas on the performance of the IT-PCFC with LSM–BCY15 cathode, while supplying dry air at the cathode, is shown in Fig. 9(A) and the observations are similar to those observed in the case of PCFC with LSM–GDC cathode. The presence of water vapor in the anode gas has no significant effect on the values of OCV but there is a small decrease in the maximum power density in the presence of humidity, which may be due to the effect of fuel dilution in the presence of humidity in the fuel. The impedance response of the IT-PCFC at OCV in Fig. 9(B) and the corresponding variations of ASR with the variation of P_{H_2O} in anode gas are also given in Table 2. Even with the LSM–BCY15 cathode, there is an increase in the electrode ASR in the presence of water vapor in the anode gas. However, the comparison of the results in Figs. 8 and 9 again shows that the IT-PCFC with LSM–BCY15 cathode has better performance than that with LSM–GDC cathode in the presence of humidity in the anode gas, which was expected from the results in the dry atmosphere in Section 3.2.1.

3.2.4. Effect of the presence of water vapor in the anode and cathode gases

Following the trend of our discussion in previous sections, we select two different cathodes: (1) LSM–GDC and (2) LSM–BCY15

while studying the effect of the presence of water vapor in the anode gas as well as in the cathode gas. The fuel cell tests are performed with LSM–GDC cathode using a cell assembly (9) given below, and with LSM–BCY15 cathode, the fuel cell tests are performed using a cell assembly (10) given below,

Wet H_2 , NiO–BCY15|BCY15|LSM–GDC, wet air (9)

Wet H_2 , NiO–BCY15|BCY15|LSM–BCY15, wet air (10)

The effect of the presence of water vapor in the anode and cathode gases on the performance of the IT-PCFC with LSM–GDC cathode is shown in Fig. 10 and the effect of the presence of water vapor in the anode and cathode gases on the performance of the IT-PCFC with LSM–BCY15 cathode is shown in Fig. 11. As it is expected from the negative effect of the presence of humidity on the individual electrodes (cathode/anode), the presence of the humidity simultaneously in the anode and cathode gases has more pronounced effect on the fuel cell performance. In order to compare the effect of humidity on the fuel cell performance while using a particular type of cathode (LSM–GDC/LSM–BCY15), various results are compiled and are presented in Table 3. The comparison of the results, using a particular type of cathode, clearly shows that

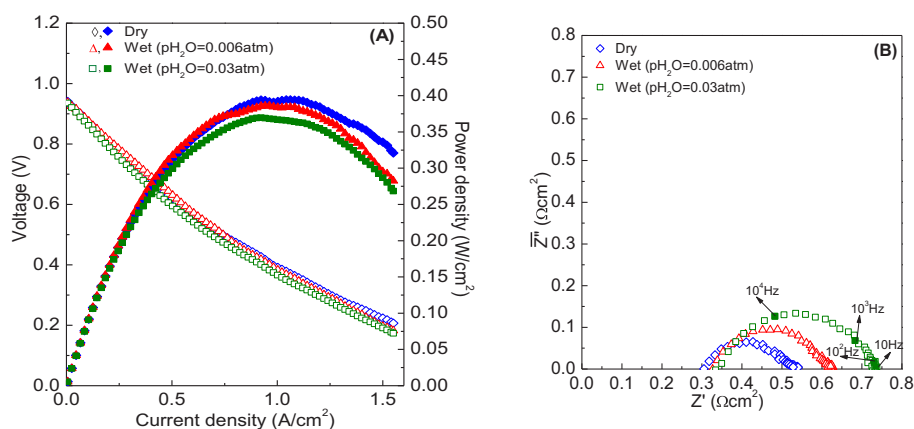


Fig. 10. Effect of simultaneous variation of humidity in anode gas (H_2 fuel) and cathode gas (air) while using LSM–GDC cathode. (A) Variation of voltage and power density vs. current density and (B) variation of EIS response. The closed symbols in (A) represent data of power densities and the open symbols represent data of the voltage. Measurements were performed at 750°C .

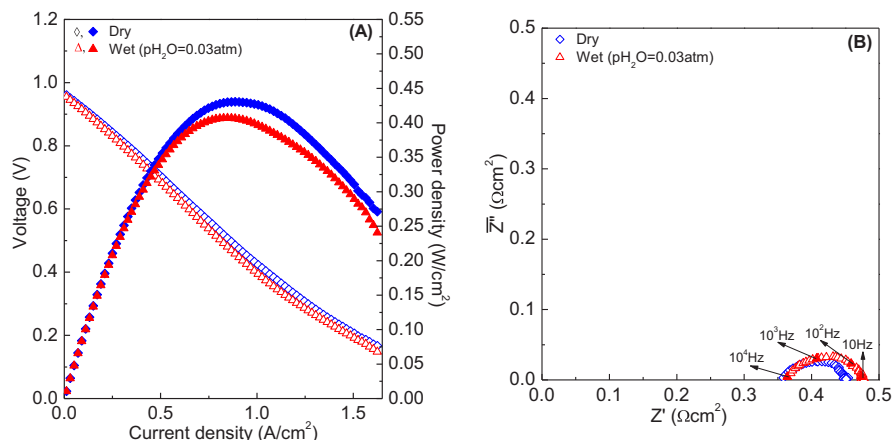


Fig. 11. Effect of simultaneous variation of humidity in anode gas (H_2 fuel) and cathode gas (air) while using LSM–BCY15 cathode. (A) Variation of voltage and power density vs. current density and (B) variation of EIS response. The closed symbols in (A) represent data of power densities and the open symbols represent data of the voltage. Measurements were performed at 750 °C.

Table 3

Effect of simultaneous variation of humidity condition of the cathode and anode gases on the various parameters of IT-PCFC performance at 750 °C.

Type of cathode	Gas condition (anode/cathode)	Theoretical OCV (V)	Measured OCV (V)	Max. power density (W cm^{-2})	Ohmic ASR ($\Omega \text{ cm}^2$)	Electrode ASR ($\Omega \text{ cm}^2$)	Total ASR ($\Omega \text{ cm}^2$)
LSM–GDC	Dry/Dry	1.358	0.941	0.394	0.298	0.233	0.530
	Wet ($\text{pH}_2\text{O} = 0.03 \text{ atm}$)/Dry	1.107	0.940	0.381	0.332	0.323	0.654
	Dry/Wet ($\text{pH}_2\text{O} = 0.03 \text{ atm}$)	1.357	0.936	0.380	0.331	0.333	0.664
	Wet ($\text{pH}_2\text{O} = 0.03 \text{ atm}$)/Wet ($\text{pH}_2\text{O} = 0.03 \text{ atm}$)	1.105	0.935	0.370	0.343	0.382	0.725
LSM–BCY15	Dry/Dry	1.358	0.961	0.430	0.356	0.099	0.455
	Wet ($\text{pH}_2\text{O} = 0.03 \text{ atm}$)/Dry	1.107	0.959	0.419	0.359	0.109	0.468
	Dry/Wet ($\text{pH}_2\text{O} = 0.03 \text{ atm}$)	1.357	0.955	0.417	0.360	0.111	0.471
	Wet ($\text{pH}_2\text{O} = 0.03 \text{ atm}$)/Wet ($\text{pH}_2\text{O} = 0.03 \text{ atm}$)	1.105	0.954	0.407	0.362	0.117	0.480

although the presence of humidity in the anode/cathode gases has adverse effect on the performance of the BCY15 electrolyte-based IT-PCFC, it is the presence of humidity in cathode gas which dominated in the overall lowering in the performance. Also, on comparing the results of LSM–GDC cathode with that of LSM–BCY15 cathode, it is clear that in all conditions BCY15 electrolyte-based IT-PCFC has better performance with LSM–BCY15 cathode than that with the LSM–GDC cathode.

4. Conclusion

The increase in flow rate of the cathode and anode gases leads to the improvements in the performance of BCY15 electrolyte based IT-PCFC. Increased flow rate of the anode gas helps better diffusion of the fuel to the TPB, which increases the effective partial pressure of the fuel at the TPB and its better utilization. Also, the increased gas flow rate at the cathode helps in rapid removal of water vapor formed during the operation of PCFC and helps in lowering the electrode ASR. The presence of humidity in the cathode/anode gases has negative effect on the performance of BCY15 electrolyte-based IT-PCFC, while using ceramic electrodes. The better performance in dry conditions confirms the mixed conducting nature of BCY15 electrolyte at 750 °C. The negative effect of humidity on the overall performance of IT-PCFC is more severe when it is present in the cathode gas than when it is present in the anode gas. Also, the effect of humidity is dependent on the nature of the cathode material and the use of LSM–BCY15 cathode in place of LSM–GDC cathode mitigates the adverse effects of humidity on the performance of the IT-PCFC at 750 °C to a certain extent.

Acknowledgments

This work was supported by Priority Research Centers Program through the National Research Foundation of Korea(NRF) funded by the Ministry of Education, Science and Technology(2009-0094055).

References

- [1] E.D. Wachsman, K.D. Lee, *Science* 334 (2011) 935–939.
- [2] D.J.L. Brett, A. Atkinson, N.P. Brandon, S.J. Skinner, *Chem. Soc. Rev.* 37 (2008) 1568–1578.
- [3] E. Fabbri, L. Bi, D. Pergolesi, E. Traversa, *Adv. Mater.* 24 (2012) 195–208.
- [4] B.C.H. Steele, *Solid State Ion.* 134 (2000) 3–20.
- [5] M.L. Far, D.L. Rosa, V. Antonucci, A.S. Arico, *J. Indian Inst. Sci.* 89 (2009) 363–380.
- [6] T. Hibino, A. Hashimoto, M. Suzuki, M. Sano, *J. Electrochem. Soc.* 149 (2002) A1503–A1508.
- [7] D.L. Rosa, M.L. Far, G. Monforte, V. Antonucci, A.S. Arico, *J. Appl. Electrochem.* 39 (2009) 477–483.
- [8] O. Paschos, J. Kunze, U. Stimming, F. Maglia, *J. Phys. Condens. Matter* 23 (2011) 234110–234135.
- [9] C.J. Park, D.H. Kim, J.K. Kim, J.S. Lee, S.J. Song, *J. Electrochem. Soc.* 156 (2009) E23–E25.
- [10] R. Haugrud, T. Norby, *Nat. Mater.* 5 (2006) 193–196.
- [11] T. Møkkelbost, O. Andersen, R.A. Strom, K. Wiik, T. Grande, M.A. Einarsrud, *J. Am. Ceram. Soc.* 90 (2007) 3395–3400.
- [12] S.S. Bhella, V. Thangadurai, *J. Power Sources* 186 (2009) 311–319.
- [13] E. Boehm, A.J. McEvoy, *Fuel Cells* 6 (2006) 54–58.
- [14] N. Maffei, L. Pelletier, A. McFarlan, *J. Power Sources* 136 (2004) 24–29.
- [15] H. Iwahara, Y. Asakura, K. Katahira, M. Tanaka, *Solid State Ion.* 168 (2004) 299.
- [16] D.K. Lim, C.J. Park, M.B. Choi, C.N. Park, S.J. Song, *Int. J. Hydrogen Energy* 35 (2010) 10624–10629.
- [17] C.J. Park, H.W. Ryu, J.H. Moon, J.S. Lee, S.J. Song, *Ceram. Int.* 35 (2009) 1769–1773.
- [18] S.J. Song, J.H. Moon, T.H. Lee, S.E. Dorris, U. Balachandran, *J. Ceram. Process. Res.* 9 (2008) 376–380.

- [19] Z. Tao, Z. Zhu, H. Wang, W. Liu, J. Power Sources 195 (2010) 3481–3484.
- [20] K. Xie, R. Yan, X. Liu, J. Alloys Compd. 479 (2009) L36–L39.
- [21] E.P. Murray, M.J. Sever, S.A. Barnett, Solid State Ion. 148 (2002) 27–34.
- [22] S.Y. Jeon, M.B. Choi, J.Y. Park, S.J. Song, J. Ceram. Process. Res. 12 (2011) 26–29.
- [23] Z. Shao, S.M. Haile, Nature 431 (2004) 170–172.
- [24] C. Xia, W. Rauch, F. Chen, M. Liu, Solid State Ion. 149 (2002) 11–19.
- [25] L. Zhao, B. He, B. Lin, H. Ding, S. Wang, Y. Ling, R. Peng, G. Meng, X. Liu, J. Power Sources 194 (2009) 835–837.
- [26] M.B. Choi, S.Y. Jeon, J.S. Lee, H.J. Hwang, S.J. Song, J. Power Sources 195 (2010) 1059–1064.
- [27] A. Lashtabeg, S.J. Skinner, J. Mater. Chem. 16 (2006) 3161–3170.
- [28] A. Atkinson, S. Barnett, R.J. Gorte, J.T.S. Irvine, A.J. Mcevoy, M. Mogensen, S.C. Singhal, J. Vohs, Nat. Mater. 3 (2004) 17–27.
- [29] Y. Aoki, Y. Fukunaga, H. Habazaki, T. Kunitake, J. Electrochem. Soc. 158 (8) (2011) B866–B870.
- [30] K. Yashiro, T. Nakamura, M. Sase, F. Hermes, K. Sato, T. Kawada, J. Mizusaki, Electrochem. Solid State Lett. 12 (2009) B135–B137.
- [31] P. Pasierb, J. Wyrwa, M. Rekas, Ceram. Mater. 62 (2010) 311–315.
- [32] K. Takeuchi, C.K. Loong, J.W. Richardson Jr., J. Guan, S.E. Dorris, U. Balachandran, Solid State Ion. 138 (2000) 63–77.
- [33] S.P. Jiang, W. Wang, Solid State Ion. 176 (2005) 1351–1357.
- [34] E.P. Murray, S.A. Barnett, Solid State Ion. 143 (2001) 265–273.
- [35] E. Fabbri, S. Licoccia, E. Traversa, E.D. Wachsman, Fuel Cells 9 (2009) 128–138.
- [36] H. Taherparvar, J.A. Kilner, R.T. Baker, M. Sahibzada, Solid State Ion. 162–163 (2003) 297–303.
- [37] J.S. Ahn, S. Omar, H.S. Yoon, J.C. Nino, E.D. Wachsman, J. Power Sources 195 (2010) 2131–2135.
- [38] J.S. Ahn, H.S. Yoon, K.T. Lee, M.A. Camaratta, E.D. Wachsman, Fuel Cells 9 (2009) 643–649.
- [39] K.T. Lee, D.W. Jung, M.A. Camaratta, H.S. Yoon, J.S. Ahn, E.D. Wachsman, J. Power Sources 205 (2012) 122–128.
- [40] J. Larminie, A. Dicks, Fuel Cell Systems Explained, second ed., John Wiley & Sons Ltd, 2003, p. 37.